PROCEEDINGS OF SPIE

SPIEDigitalLibrary.org/conference-proceedings-of-spie

Signal nonlinearity measurements and corrections in MWIR and LWIR HgCdTe H2RG arrays for NEO Surveyor

Zengilowski, Gregory, McMurtry, Craig, Pipher, Judith, Reilly, Nicholas, Forrest, William, et al.

Gregory R. Zengilowski, Craig W. McMurtry, Judith L. Pipher, Nicholas S. Reilly, William J. Forrest, Mario S. Cabrera, Meghan L. Dorn, Andre F. Wong, A. K. Mainzer, "Signal nonlinearity measurements and corrections in MWIR and LWIR HgCdTe H2RG arrays for NEO Surveyor," Proc. SPIE 11454, X-Ray, Optical, and Infrared Detectors for Astronomy IX, 1145435 (13 December 2020); doi: 10.1117/12.2563138

SPIE.

Event: SPIE Astronomical Telescopes + Instrumentation, 2020, Online Only

Signal nonlinearity measurements and corrections in MWIR and LWIR HgCdTe H2RG arrays for NEO Surveyor

Gregory R. Zengilowski[a], Craig W. McMurtry[a], Judith L. Pipher[a], Nicholas S. Reilly[a], William J. Forrest[a], Mario S. Cabrera[b], Meghan L. Dorn[c], Andre F. Wong[d], and A. K. Mainzer[d]

[a]University of Rochester, Department of Physics and Astronomy, 500 Wilson Blvd., Rochester, NY, USA 14627
[b]Conceptual Analytics LLC, 8209 Woburn Abbey Rd., Glenn Dale, MD, USA 20769
[c]Teledyne Imaging Sensors, 5212 Verdugo Way, Camarillo, CA, USA 93012
[d]University of Arizona, Lunar and Planetary Sciences Laboratory, 629 E. University Blvd., Tucson, AZ, USA 85721

ABSTRACT

The depletion region around each *p-n* junction in HgCdTe HAWAII-2RG detector arrays decreases in volume as charge is collected, causing the pixel capacitance to change continuously throughout an integration period. This changing capacitance manifests as a steadily decreasing measured signal rate while observing a constant flux. Ignoring this nonlinear response to signal accumulation can lead to underestimating the number of detected photons by as much as 10%. Presented here are two methods, one simple and one complex, of measuring this signal nonlinearity and a theoretical framework behind a nonlinearity correction method. Additionally, experimental data are compared with simulations to explain methods to reduce noise in the nonlinearity measurement and identify deviations from the expected behavior that merit further study.

Keywords: Nonlinearity, HgCdTe, Nearest Neighbor Interactions, LWIR, MWIR, Infrared Detector

1. INTRODUCTION

The Near-Earth Object Surveyor (NEO Surveyor), which was previously known as the Near-Earth Object Camera[1] (NEOCam), is a NASA mission currently in the formulation phase designed to discover and characterize asteroids and comets that may pose potential hazards to Earth. This mission would also provide information about the origin and fate of near-Earth objects (NEOs), assess our risk from impacts, and identify targets for future manned or robotic missions. Although NEO Surveyor will be able to detect NEOs as small as 10 m, which typically exhibit behavior like the surprise airburst that occurred in Chelyabinsk, Russia[2] in 2013, NEO Surveyor will focus on pursuing completeness for objects larger than 140 m in diameter. This size selection is based on a 2005 directive by the United States Congress[3] requiring NASA to identify 90% of NEOs with diameters larger than 140 m and a perihelion distance smaller than 1.3 Astronomical Units (AUs). A catalog of this population corresponds to retiring 90% of the risk of regional, sub-global effects, along with 99% of the overall risk to human populations as a result of an unexpected impact.[4] NEO Surveyor expects to identify greater than 2/3 of these NEOs during its five year baseline mission.[5]

To illustrate the importance of a mission such as NEO Surveyor, asteroid 2019 OK was detected for the first time[6] in July 2019 one day before narrowly missing the Earth. At its closest approach, this asteroid was separated from the Earth by[7] 4.8×10^{-4} AU, or a fifth of the Earth-Moon distance. 2019 OK is similar in size to the impactor believed to cause the Tunguska event,[8] which flattened over 2000 km^2 of forest in an airburst explosion on the order of 12 Megatons of TNT, 25 times larger than the airburst observed in Chelyabinsk.[2] Using the known orbit of 2019 OK and the planned NEO Surveyor survey strategy, 2019 OK would very likely

Further author information: (Send correspondence to G.R.Z.)
G.R.Z.: E-mail: g.zengilowski@rochester.edu

X-Ray, Optical, and Infrared Detectors for Astronomy IX, edited by Andrew D. Holland, James Beletic, Proc. of SPIE Vol. 11454, 1145435 · © 2020 SPIE
CCC code: 0277-786X/20/$21 · doi: 10.1117/12.2563138

have been detectable in 2017. A two-year advanced warning, which might allow for intervention if necessary, is significantly more desirable than the 24 hour notice that occurred in July 2019.

NEO Surveyor builds upon the asteroid-detecting experience from the NEOWISE survey.[9] The larger 0.5 cm primary will provide greater sensitivity and NEO Surveyor will have a much larger field of view than its predecessor (11.56 square degrees[1] compared to 0.61 square degrees[10]). In addition, its position at the Earth-Sun L1 Lagrange point will provide a cold working environment facilitating full passive cooling for the instrument, while still allowing for high-bandwidth downlinks. Another major advancement for NEO Surveyor is the recent development in infrared detector technologies. NEO Surveyor will use two infrared wavelength channels, a mid-wave infrared (MWIR) channel, NC1, covering the 4-5.2 μm wavelength range and a long-wave infrared (LWIR) channel, NC2, covering the 6-10 μm range. Both channels will use four HAWAII-2RG (H2RG) HgCdTe arrays.[11] Detectors for the NC1 channel have been sufficiently developed for missions such as the James Webb Space Telescope[12] (JWST) and little new work is required on these detectors for NEO Surveyor. The LWIR NC2 detectors, however, are the result of a collaborative design effort by the University of Rochester, the University of Arizona, the Jet Propulsion Laboratory (JPL), and Teledyne Imaging Sensors (TIS) extending from single pixel devices produced in 1994 to the 2048x2048 pixel H2RG format to be used with NEO Surveyor. The LWIR detector development was funded by a series of NASA technology development grants. These detectors are vastly preferable to other LWIR options as they can operate at temperatures as high[12] as 42 K, which are achievable by passive cooling, while satisfying the NEO Surveyor requirements. Other LWIR options, such as the Arsenic-doped Silicon (Si:As) detectors used in the Spitzer Space Telescope and the Wide-Field Infrared Survey Explorer[10] (WISE), and to be used with the Mid-Infrared Instrument[13] (MIRI) for JWST, require operating temperatures below 8 K, often using cryocoolers or solid hydrogen or liquid helium as a cryogen.[1] Cryogens increase the cost and weight of a mission and significantly limit the lifetime based on the amount launched with the satellite.

During the formulation phase, the NEO Surveyor detector team has been focused on preparing for the flight production of MWIR and LWIR Sensor Chip Assemblies (SCAs). TIS has fabricated several flight-like "flight pathfinder" SCAs and engineering-grade SCAs for both the MWIR and LWIR channels. With these detectors, the University of Rochester has also performed detailed performance testing of detector properties relevant to NEO Surveyor, some of which are presented in this paper.

For these arrays, molecular beam epitaxy (MBE) is used to grow the HgCdTe crystal on a CdZnTe substrate. Growing the HgCdTe detector material on CdZnTe requires fine-tuning of the Cd to Zn ratios in the substrate to match the desired lattice spacing of the detector crystal. Poorly matched substrates cause strain within the detector layer, which is released through defects in the grown crystal. These defects typically occur along intersections of the (211) growth plane and the eight HgCdTe slip planes.[14] Surface defects, such as voids and screw or misfit dislocations, create cross-hatching patterns of lines parallel to the $[\bar{2}13]$, $[\bar{2}31]$, and $[0\bar{1}1]$ crystallographic directions.[15] The $[0\bar{1}1]$ line can vanish entirely under optimal growth conditions[16] and exhibits different behaviors from the equivalent[16] $[\bar{2}13]$ and $[\bar{2}31]$ lines.

Although these effects are accentuated when moving to longer wavelengths, the Rochester Group and TIS have had success tackling these issues while extending this detector technology beyond the 10 μm cutoff wavelength for NEO Surveyor to 13 μm and 15 μm for potential future missions.[17,18] Increasing the mercury/cadmium ratio in the material increases the cutoff wavelength, but it also makes the material softer and more susceptible to strain related defects because of the relatively weak HgTe bonds.[15] The smaller band gap energy also makes it easier for electrons to be excited across the band gap through thermal motion or quantum tunneling, leading to larger dark currents. Traps associated with defects that preferentially fall along the cross-hatching lines can facilitate especially large trap-assisted tunneling dark currents. It is these trap-assisted tunneling currents that typically limit the operability of NEO Surveyor arrays. The current NEO Surveyor operability requirements include specifications on the dark current, well depth, read noise, and quantum efficiency of each pixel. For the sake of simplicity, only the dark current and well depth requirements will be used here in identifying operable and inoperable pixels. Using this operability definition, any pixel with an initial dark current larger than 200 e-/s or a well depth smaller than 44,000 e- is marked as inoperable. Pixels that fail the well depth requirements are typically pixels with large dark currents that lose significant portions of their well depth between resetting the pixel and reading it for the first time. These operability requirements are depicted graphically as the horizontal

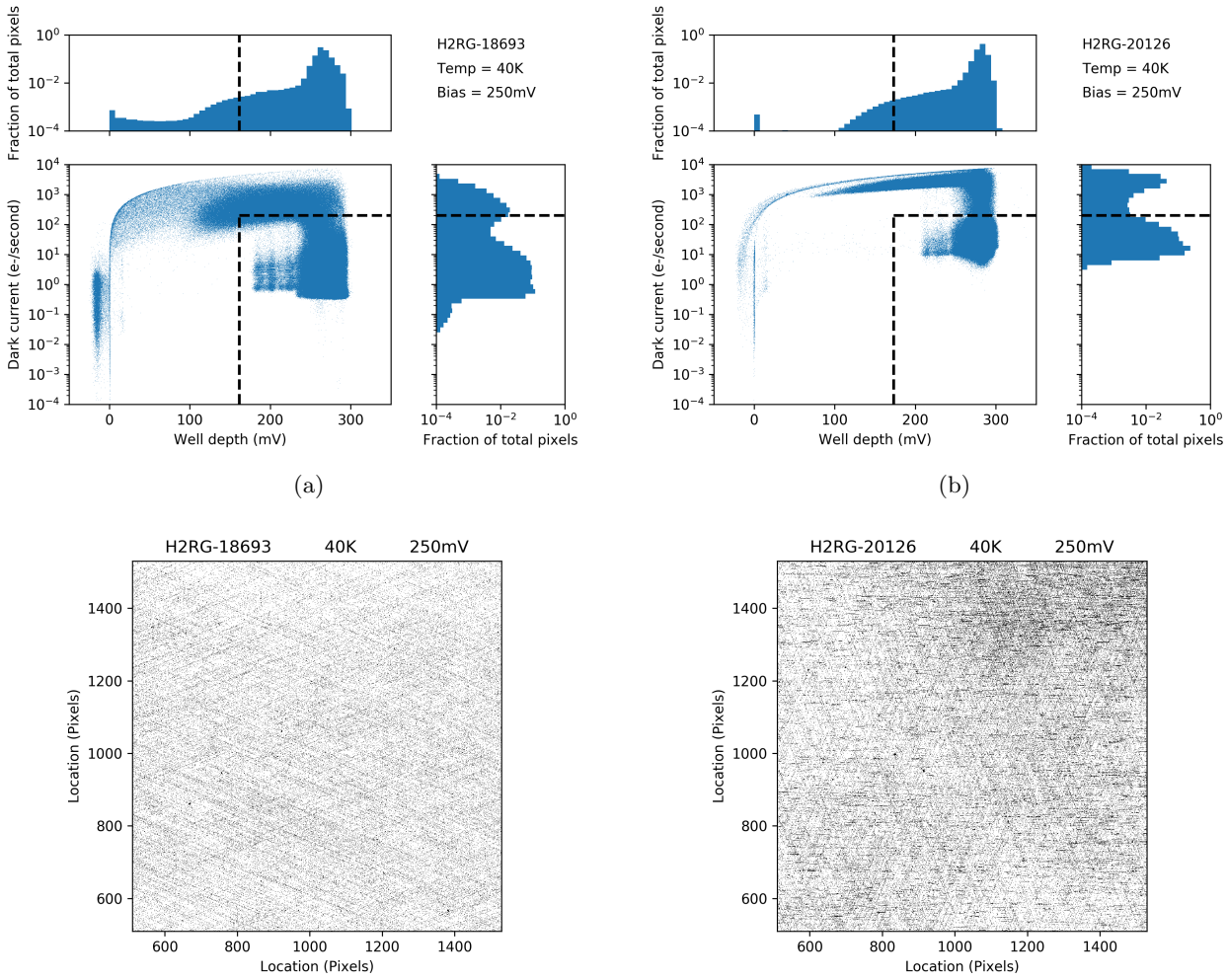

Figure 1: Measured dark current and well depth values for all 4 million pixels in (a) H2RG-18693, a well-performing engineering-grade SCA with a cutoff wavelength of 9.9 μm and (b) H2RG-20126, a poor-performing engineering-grade SCA with a cutoff wavelength of 10.2 μm. The dark current requirement of 200 e-/s is depicted as the horizontal dashed line and the well depth requirement of 44,000 e- at 250 mV of applied bias is shown as the vertical dashed line. Pixels that fall below and to the right of these two lines are marked as operable and all other pixels are marked as inoperable. Operability maps showing the inoperable pixels in black for the central 1024 pixel x 1024 pixel region of (c) H2RG-18693 and (d) H2RG-20126. The map for H2RG-18693 shows the presence of the $[\bar{2}13]$ and $[\bar{2}31]$ cross-hatching lines as the lines splitting the horizontal with a 44.4° degree[14,16] angle between them. The $[0\bar{1}1]$ line, which would appear as a vertical line in this map, is noticeably absent. All three lines can be seen in the map for H2RG-20126, albeit rotated by 90° because of the detector crystal orientation relative to the readout circuitry.

and vertical dashed lines respectively in Fig. 1a and Fig. 1b, which show the dark current and well depth measurements for all pixels in H2RG-18693, an array with a 9.9 μm cutoff wavelength, and H2RG-20126, a 10.2 μm cutoff array. Operability maps, such as those shown in Fig. 1c and Fig. 1d, which depict pixels that fail the operability requirements in black, clearly show the preference for inoperable (high dark current) pixels to fall along cross-hatching lines.

Every pixel in a H2RG array is constructed by inserting a p-type implant into the n-type bulk material,

forming a p-n junction. Extra electrons from the n-type side diffuse to the p-type side where they recombine with the extra holes. The ensuing separation of charges creates a region around the junction depleted of majority carriers, known as the depletion region, and establishes an electric field throughout this region. Applying a voltage across the junction changes the width of this depletion region, with a reverse bias (larger voltage attached to the n-type side) creating a larger depletion region by pulling extra electrons away from the junction towards the positive voltage source. H2RG arrays are operated under reverse bias and move towards zero bias as charges are collected before eventually saturating, if given enough time, either at zero bias if in the dark or in forward bias if illuminated.

When a photon is absorbed within the detector layer, an electron-hole pair is generated. These charges randomly walk throughout the bulk material and if the hole encounters the electric field in the depletion region, it is swept across the junction. In doing so, it reduces the amount of separated static charge and, as a result, decreases the voltage across the junction, the depletion electric field, and the width of the depletion region.

During operation, the array can be read nondestructively by measuring the voltage across each pixel. The quantity desired by most users of H2RG arrays is not voltage, however, but the number of collected charges. The measured voltage changes across an integration time can be converted to the number of detected electrons through the use of a conversion factor with units of charge/voltage, which is a capacitance. Unfortunately, because of the decreasing depletion electric field and decreasing depletion region width, every subsequent charge that is swept across the junction produces a smaller voltage change ($\Delta V = \int E \cdot \mathrm{d}x$) than the charges that came before it. This nonlinear response to signal accumulation behaves as a continuously increasing capacitance and ignoring this behavior can lead to drastically underestimating the total number of photons detected during an integration period.

2. SAMPLING AND CALIBRATION

Two sampling methods are used for this analysis. The first method,[19] known as correlated double sampling (CDS), involves reading the detector twice nondestructively separated by a desired integration time. The first read, known as the pedestal frame, serves as the zero-point for the integration, and is subtracted from the second read producing a single CDS image that shows the net change in voltage across every pixel throughout the integration time. The LWIR channel for NEO Surveyor, NC2, is planning to use this sampling method and to download an average of eight CDS images taken in rapid succession at each dither location. The second method,[20] known as sample-up-the-ramp (SUTR) sampling involves taking multiple reads nondestructively, allowing for study of the pixels' evolution at various points throughout the total integration time. NC1, the MWIR channel for NEO Surveyor, is planning to use this sampling method and to download only an image of the signal vs. time slopes for the full integration ramp of 18 frames taken at each dither location. For all SUTR sets included here, the first frame is subtracted from every subsequent frame to serve as a baseline zero-point for the full ramp. Each read of the array shows the voltage across every pixel in the detector and these voltages are reported in analog-to-digital units (ADUs), where 1 ADU in a CDS image corresponds to a change of 7.7 μV across the pixel using the current Rochester experimental set up.

The array capacitance can be measured to convert these measured voltages to electrons using the noise squared vs. signal method[21] and values on the order of 2 e-/ADU are typical. This value is an overestimate by as much as 10% due to a nearest neighbor interaction[22] known as interpixel capacitance (IPC), which blurs the image reducing the noise without influencing the signal under uniform illumination. To correct for this effect, the IPC correction factor is measured using the hot pixel method.[23] Additionally, this capacitance is bias-dependant. It increases throughout the integration time, leading to a continual decrease in the measured voltage signal rate for a constant photon flux. Using a constant capacitance can lead to underestimating the actual number of charges collected by about 10% when operating near the well depth. Instead, the signal nonlinearity should be measured and corrected to ensure a more accurate count of the detected photons.

3. DETECTING AND MEASURING SIGNAL NONLINEARITY

The signal nonlinearity can be observed by staring at a constant light source for a long SUTR ramp and plotting average signal rate (total signal in frame/total integration time to frame) vs. time or signal for every frame in

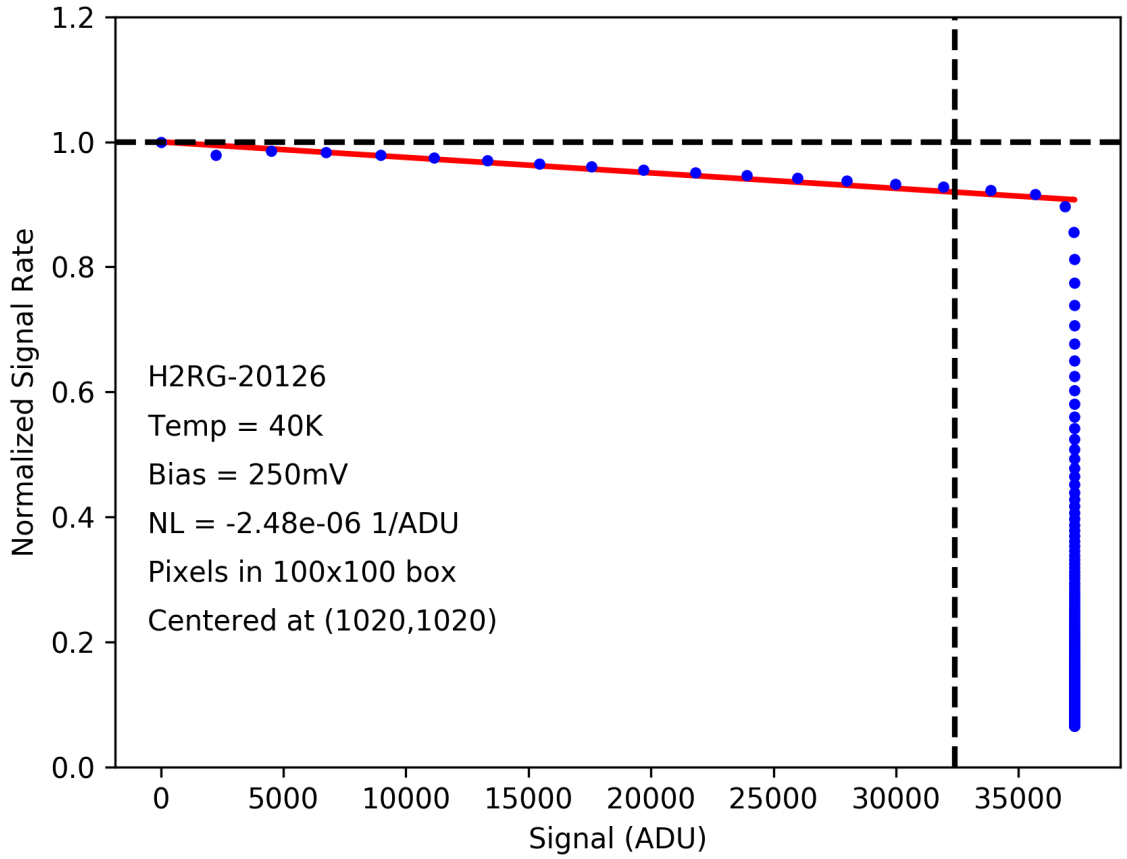

Figure 2: Average signal rate, total signal divided by total time, for 250 frames of a SUTR integration looking at a dim, constant flux. The blue points represent the median signal rate of all pixels in a central 100x100 pixel box for each frame of the ramp. The signal rate is normalized to the intercept of the red line, so the horizontal line at a normalized signal rate of 1 represents the expected signal rate if the capacitance had been constant throughout the ramp. The vertical dashed line marks a change of 250 mV, the applied reverse bias, from the pedestal frame. Data points continue past this value because of a pedestal injection on the order of 30 mV due to stray capacitances in the circuitry unit cell of each pixel and because pixels saturate in forward bias. The signal rate is plotted against signal for ease of correcting for nonlinearity. The difference between the red line and the horizontal line at a normalized signal rate of 1 is the fraction of signal "lost" due to the changing capacitance. NL, the slope of the red line, is the measured nonlinearity of the array.

the ramp. An example of this flux vs. fluence (FF) curve is shown in Fig. 2. In this figure, the horizontal dashed line at a normalized signal rate of 1 represents the expected signal rate if the capacitance was constant throughout the integration time. Instead of following this behavior, the voltage signal rate decreases throughout the integration time as the capacitance continually increases.

Treating this decreasing signal rate as "lost" signal leads to an easy method of measuring and calibrating this signal nonlinearity. Assuming a signal value M is measured after some integration time t and the expected signal from the ideal constant capacitance behavior is E, then the fraction of total signal that is missing can be expressed as

$$f = \frac{E - M}{E}. \tag{1}$$

This fraction can be rewritten using the time-averaged fluxes, F_M and F_E, that produced M and E respectively as

$$f = \frac{F_E t - F_M t}{F_E t} = \frac{F_E - F_M}{F_E} = 1 - \frac{F_M}{F_E}. \tag{2}$$

The data points in Fig. 2 represent F_M/F_E, the average signal rate needed to produce the measured signal normalized to the initial signal rate. As shown in Eq. (2), the difference between the horizontal line at a normalized signal rate of 1 and these data points represents the fraction of signal lost as a function of measured signal in a CDS image. As these data follow a linear relationship, the curve of F_M/F_E can be expressed as

$$\frac{F_M}{F_E} = 1 + NM, \tag{3}$$

where N, the slope of the red line in Fig. 2, is the measured signal nonlinearity. Rearranging Eq. (1) and using the simple linear model in Eq. (3) with Eq. (2) allows for a simple correction from the original measured signal M to the nonlinearity corrected signal E using

$$E = \frac{M}{1 + NM}. \tag{4}$$

CDS images, which will be used in the NEO Surveyor LWIR channel, can easily be corrected using the measured signal values in the CDS images with Eq. (4). The MWIR channel for NEO Surveyor, however, will only download a single image of the measured slopes for each SUTR integration. Despite only having access to the measured slope of the uncorrected signal values vs. time, a similar correction method can be used to correct data from this channel. Assuming the measured slope is F_M for a ramp with Z frames taken throughout the ramp, each separated by an integration time t, then the signal expected in the z-th frame can be calculated as $M_z = ztF_m$. Each of these expected signal values can be corrected for nonlinearity with Eq. (4), and the resulting nonlinearity corrected slope F_E can be calculated as the result of a linear fit using

$$E_z = \frac{ztF_m}{1 + ztNF_m} \qquad F_E = \frac{Z(\sum_{z=1}^{Z} ztE_z) - (\sum_{z=1}^{Z} zt) \times (\sum_{z=1}^{Z} E_z)}{Z(\sum_{z=1}^{Z} (zt)^2) - (\sum_{z=1}^{Z} zt)^2}. \tag{5}$$

Three examples of this correction are shown in Fig. 3 for the 5.7 μm cutoff NC1 array H2RG-20909, along with the FF curves used to measure the nonlinearities N for each of the three pixels of interest. In all three cases, the resulting nonlinearity corrected slope matches both the slope measured using a linear fit of the signal values corrected using Eq. (4) and the initial signal rate measured using the flux vs. fluence method.

Both of these correction methods require a process to measure the signal nonlinearity N. For typical array characterization, a simple method that produces a single array-wide value is frequently used. In this method, a dim light source is observed for a long SUTR ramp to ensure the majority of pixels reach saturation. A FF curve, like that shown in Fig. 2, albeit unnormalized, is created for every pixel that sees a voltage change larger than the applied reverse bias. A linear fit is performed on this curve for the points falling between 20% and 80% of the applied bias, hereafter referred to as the 20-80% range. The measured nonlinearity for each pixel is then calculated as the slope of this linear fit divided by the y-intercept, which represents the initial signal rate and serves as the normalization constant for the FF curves. The array-wide nonlinearity is then selected as the peak of a distribution of the individual measured nonlinearities to choose a value representative of the largest number of pixels. This modal value is used because of the asymmetric nature of the histogram to shallower nonlinearities, as shown in Fig. 4, caused by deviations from the expected behavior, which will be discussed later, that skew more conventional choices such as the median.

Comparing the experimental FF curves for individual pixels with simulated curves illustrates a few important points about this measurement method. Figure 5a shows the FF curves for all pixels in the array H2RG-18693 that have measured nonlinearity values that match the median array-wide nonlinearity value with two different source intensities and Fig. 5b shows 100,000 simulated FF curves for identical pixels with similar dark current,

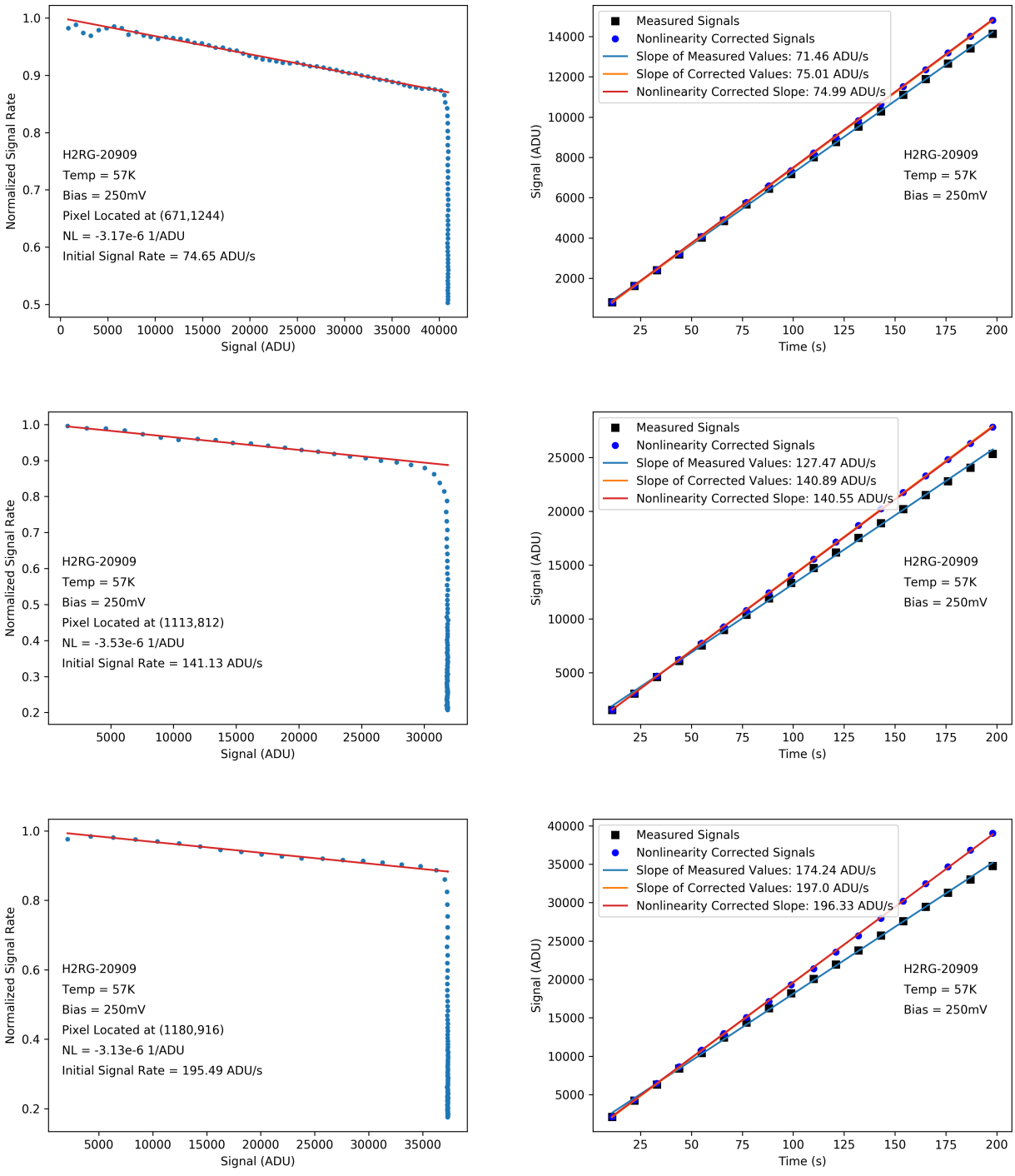

(a) (b)

Figure 3: (a) Nonlinearity measurements with different light intensities for three pixels in H2RG-20909, a 5.7 μm cutoff SCA. (b) Measured signal values and nonlinearity corrected signal values for the same three pixels. Correcting the slope of the measured signal values reproduces the slope of the nonlinearity corrected signal values.

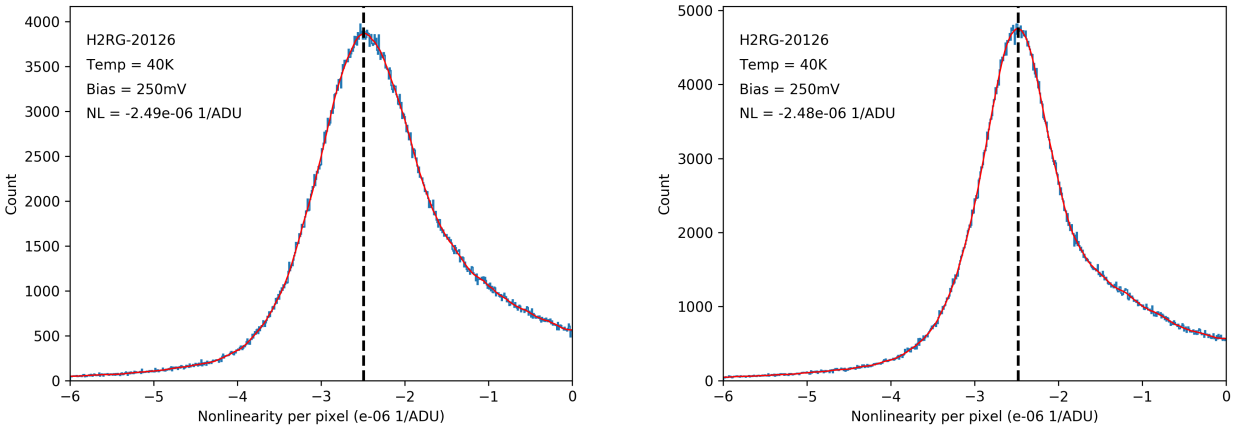

(a) (b)

Figure 4: A histogram of the measured nonlinearity values for (a) a single trial and (b) averaging the measured nonlinearity values for three separate trials in H2RG-20126, a 10.2 μm cutoff H2RG array. In both figures, the red curve is the result of passing the distribution through a Savitzky-Golay filter, and the nonlinearity value selected is the peak of the smoothed distribution. Averaging the measured values across the three trials narrows the histogram because of the reduction of correlated Poisson shot noise.

signal nonlinearity, and source flux values as observed in the measured curves. The simulations assume only a nonlinear behavior of signal accumulation governed by Eq. (4) and Poisson photon shot noise. Low signal behavior of the FF curves is dominated by Poissonian noise and the amplitude and extent of the low signal behavior seen in the experimental curves is well matched by the simulations. The broadening of the saturation level seen in the experimental curves are caused by inhomogeneities among pixels, which are not included in the simulated curves that involve identical pixels. Similarly, an unanticipated high signal deviation where the FF curves turn up from the expected behavior they had previously been following is only seen in the experimental data, suggesting an additional physical effect not included in these simple simulations.

The final important distinction between the experimental results and the simulations involves the thickness of the black bulk curves throughout the 20-80% range used to measure the nonlinearity. In the experimental curves seen in Fig. 5a, the black bulk curve pinches down faster than in the simulated curves found in Fig. 5b. This is an artificial behavior caused by a selection effect as only FF curves matching a specific selected nonlinearity value are included. Because the noise within a single ramp is correlated, a pixel whose FF curve starts at the top edge of the bulk black curve shown on the bottom of Fig. 5b is likely to "surf" along the top edge of the bulk curve as the noise decays away. Fitting a straight line to such an FF curve in the 20-80% range, depicted as the blue points, would have a steeper measured nonlinearity, and thus not be included in the plot of experimental FF curves. This leaves only well-behaved FF curves and the curves of pixels whose FF curves start noisily but rapidly decay to a better behaved level by the 20% limit, appearing as a rapid pinching of the noise. Crucially, this is not a difference in nonlinear behavior, as all of the simulated curves use identically the exact same signal nonlinearity, but instead is correlated photon shot noise influencing the measured nonlinearity. The only way to reduce this correlated noise is to take multiple ramps and compare the values for each pixel. Figure 4a shows the distribution of measured nonlinearity values for individual pixels using a single ramp and Fig. 4b shows the distribution resulting from averaging the results of three nonlinearity measurements for each pixel involving three separate ramps. The narrowing of the histogram is due to a reduction in correlated photon noise.

In the interest of studying the behavior of individual pixels, it is possible to get more precise values for a single pixel's nonlinearity by using a more complex method. Multiple trials are again used to reduce noise and a more complex point selection method is used rather than relying on the 20-80% range. Point selection begins when the second derivative of the FF curve is consistently close to zero to avoid curvature at low signals caused by noise and bias-dependent tunneling currents and stops when the pixel of interest or any of its neighbors

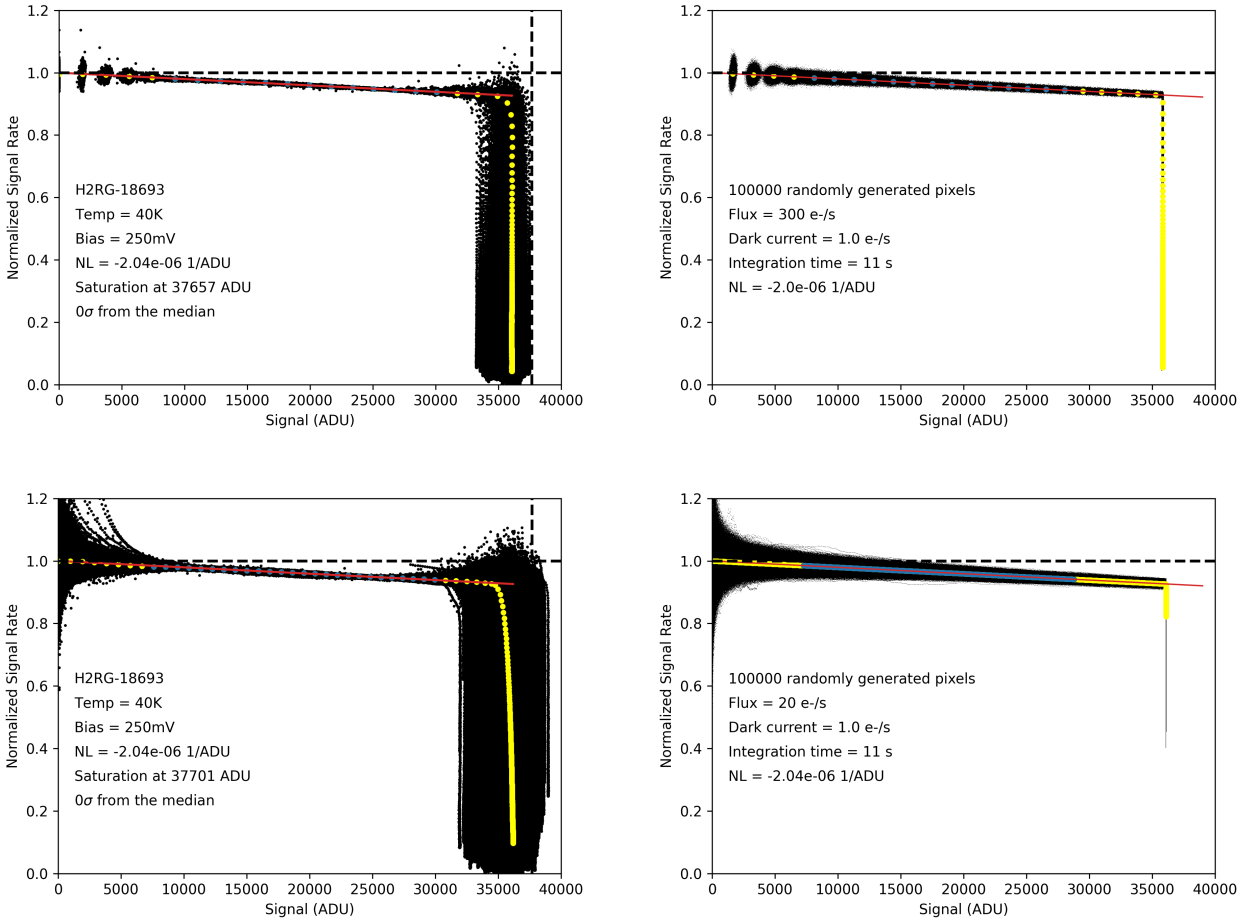

(a) (b)

Figure 5: (a) Experimental FF curves for all pixels with nonlinearity values matching the median array-wide nonlinearity in H2RG-18693 for two different light source intensities. (b) Simulated FF curves using similar dark current, signal nonlinearity, and source flux values as encountered in the two experimental curves in (a). In all figures, the black points are individual measurements, the yellow points represent the median signal and normalized signal rate values for each frame, the blue points mark the 20-80% range, and the red line shows the expected FF behavior. The low signal behavior is well matched between the simulated and experimental data, and is caused by Poisson shot noise. The few experimental FF curves with low signal behavior well above the bulk noise curves are caused by pixels with large initial tunneling currents, which decay throughout the integration. The high signal behavior where some FF curves turn up from the expected behavior is unexplained by the simulations, suggesting a physical mechanism beyond Poisson statistics and the signal nonlinearity governed by Eq. (4). Finally, the experimental bulk, black curves pinch down faster than the simulated curves because of an artificial selection effect caused by only selecting curves whose fitted slopes using points in the 20-80% range match a specific value. This excludes pixels whose measured nonlinearity value is skewed by slowly decaying correlated noise. The anomalous upturn begins after the 80% level because of a similar artificial selection effect.

accumulate signal larger than the applied bias to avoid anomalous high signal behaviors which will be explained later.

For this method, unnormalized FF curves are generated for the pixel of interest and the nonlinearity, n_l, and its uncertainty, $\sigma_{n,l}$, for the l-th included trial ramp are measured using the K selected points with an analytical linear fit as

$$n_l = \frac{\alpha\beta - \gamma^2}{\gamma p - \alpha q} \qquad \sigma^2_{n,l} = (2a^2c^2 + b^2)n^4, \tag{6}$$

where

$$\begin{gathered} F_{M,k} = \tfrac{M_k}{t_k} \qquad \sigma_k^2 = g_e M_k + I t_k + \sigma_r^2, \qquad w_k = \tfrac{2g_e^2 M_k^2}{\sigma_k^2} \\ \alpha = \textstyle\sum_{k=1}^K w_k F_{M,k}^2 \qquad \beta = \sum_{k=1}^K w_k \qquad \gamma = \sum_{k=1}^K w_k F_{M,k} \\ p = \textstyle\sum_{k=1}^K w_k M_k F_{M,k} \qquad q = \sum_{k=1}^K w_k M_k \qquad r = \sum_{k=1}^K M_k^2 \\ a = \sqrt{\tfrac{2\beta r}{\alpha\beta - \gamma^2}} \qquad b = \sqrt{\tfrac{2\alpha r}{\alpha\beta - \gamma^2}} \qquad c = \tfrac{\gamma p - \alpha q}{\beta p - \gamma q}. \end{gathered} \tag{7}$$

The sums in Eq. (7) include the K selected measurements of signal, M_k, which are measured in the k-th frame of a ramp with a net integration time t_k to reach that frame, for a pixel with measured dark current I, zero-mean read noise σ_r, and e-/ADU conversion g_e.

Once the nonlinearity n_l for each trial has been calculated, the final pixel nonlinearity is calculated as a weighted mean using the nonlinearity values n_l from each of the L included trials as

$$N = \frac{\sum_{l=1}^L w_l n_l}{\sum_{l=1}^L w_l} \qquad \sigma_N^2 = \frac{1}{\sum_{l=1}^L w_l} \qquad w_l = \frac{1}{\sigma_{n,l}^2}. \tag{8}$$

This method allows for a linear fit of the flux vs. fluence curves where the higher signal value points, which are better behaved, are weighted more heavily and produces an uncertainty for each individual trial facilitating removal of outliers through the weighted mean. Although useful for eliminating outliers, the uncertainty produced by this method is not a conventional uncertainty. It is best described as a relative level of confidence when comparing two fits because it ignores some intrinsic characteristics of the system, such as the exact dependence between the signal and signal rate in the FF curves and the strong correlation between consecutive data points. Three examples of nonlinearity measurements using this method are shown in Fig. 6. Figure 6a exhibits diverging behavior at low signal values caused by Poisson noise before decaying to the expected behavior. Tunneling dark currents are bias-dependent and as a result they decay throughout the course of an integration. In FF curves, they manifest as large signal rates that rapidly decay to the expected FF curve behavior, as is shown in Fig. 6b. Point selection is crucial for the measurement process for these two cases to ensure any undesirable behavior is excluded from the linear fit of the FF curve. Additionally, with more points included in the fit, the calculated uncertainty decreases, which allows for better behaved trials to be weighted more heavily than noisy trials when combining the results through a weighted average. Finally, in Fig. 6c, a cosmic ray hits the pixel during one of the trials, producing an obviously incorrect nonlinearity measurement for that trial. Due to the smaller number of points selected in the fit, the outlier trial ($\times$) is essentially ignored by the weighted mean and the selected nonlinearity value for the pixel (red line) matches the better behaved trial. With the ability to study the signal nonlinearity of individual pixels, it is possible to flag and identify deviations from the expected behavior that merit further study.

4. DEVIATIONS FROM EXPECTED FF BEHAVIORS

First, to look for explanations behind pixel-to-pixel variations of the measured pixel nonlinearity, Fig. 7 includes several standard deviation maps, which show the number of standard deviations a pixel's measured nonlinearity value is from the median array-wide value. In these maps, steeper nonlinearities are shown in blue and shallower nonlinearities in red. Figure 7a shows the center of the standard deviation map for H2RG-18693. Pixels with steeper nonlinearities appear preferentially along the [$\bar{2}$13] and [$\bar{2}$31] cross-hatching lines, which are also seen in Fig. 1c. This suggests steeper nonlinearities are associated with pixels that have large trap-assisted tunneling

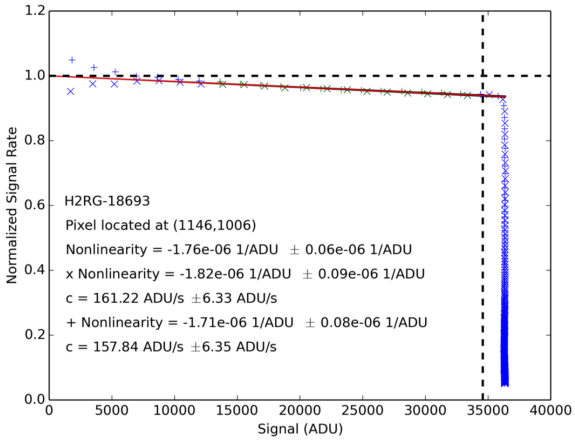

(a)

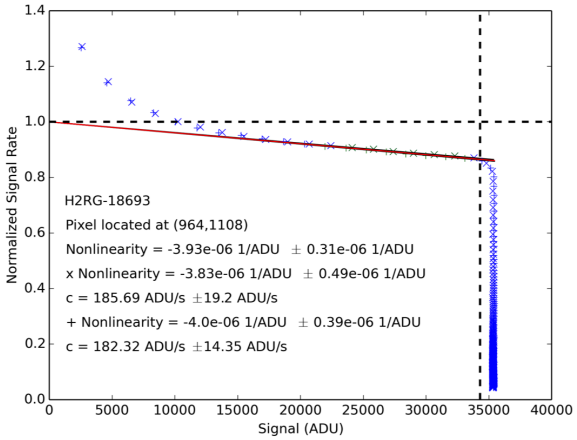

(b)

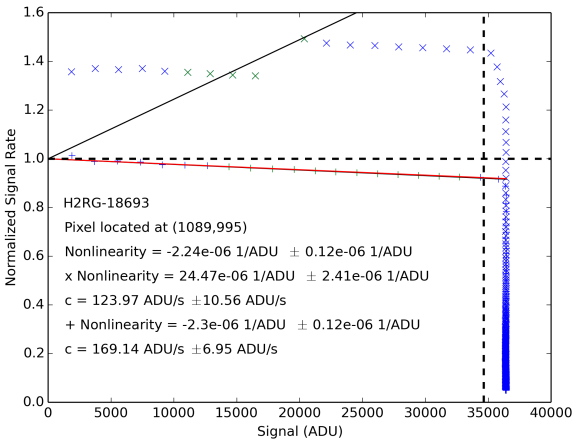

(c)

Figure 6: Examples of the complex nonlinearity measurement method using two separate trial ramps. In each figure, the two black lines show the measured nonlinearities for each trial and the red line is the weighted average of the two trials. The parameter c is the normalization constant and is calculated using Eq. (7). The vertical dashed line shows each pixel's measured well depth. Data continue past this line because pixels saturate in forward bias. (a) Nonlinearity curves exhibiting diverging low signal noise behavior. Point selection based on the second derivative excludes these low signal points from the linear fit. (b) Nonlinearity curves for a pixel with large tunnelling dark currents that are bias-dependent. Point selection based on the second derivative ignores these points and waits for the curve to decay to the expected linear behavior. (c) A case where an outlier trial that is hit by a cosmic ray (×-trial) is ignored by the weighted mean approach and the pixel nonlinearity (red line) matches the better behaved trial.

dark currents, such as is seen in Fig. 6b. Pixels with shallower nonlinearities appear, instead, in clumps distributed throughout the array. Zooming in on a portion of this map, as is depicted in Fig. 7b, shows the pixels with the largest positive standard deviation (bright red) occur exclusively around pixels that fail the NEO Surveyor dark current operability requirements, which are depicted in black. The plus-sign shape exhibited by these pixels in bright red is a characteristic signature of a nearest neighbor interaction where a central pixel shares signal with its immediate neighbors. Pixels in this standard deviation bin have measured nonlinearities of zero or larger, following an idealized "constant capacitance" behavior.

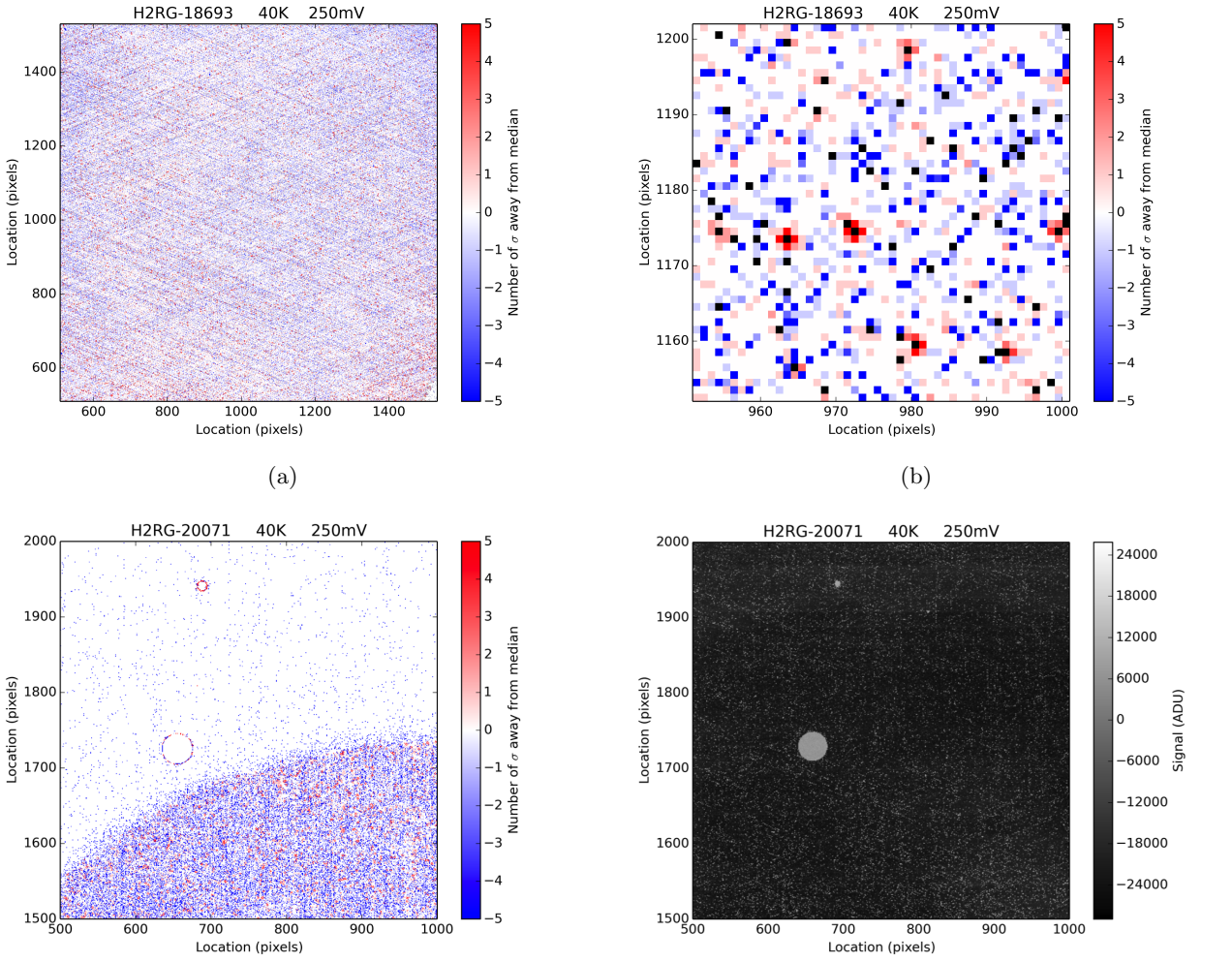

Figure 7: Maps showing the number of standard deviations a pixel's nonlinearity is from the median array-wide value ((a)-(c)) and a pedestal image taken in the dark (d). (a) The standard deviation map for H2RG-18693. Steeper nonlinearities, blue, appear preferentially on the $[\bar{2}13]$ and $[\bar{2}31]$ cross-hatching lines, which can also be seen in Fig. 1c, suggesting steep nonlinearities are tied to pixels with large tunneling dark currents, like that seen in Fig. 6b. (b) Pixels with zero measured nonlinearity, which follow the idealized "constant capacitance" behavior, are depicted as bright red and occur exclusively around pixels that fail the NEO Surveyor dark current and well depth requirements, depicted as black. The plus-sign shape exhibited by these pixels is a characteristic mark of a nearest neighbor interaction. (c) A portion of the standard deviation map for H2RG-20071, a 10.1 μm cutoff engineering-grade array. Outside the central illumination pattern, a portion of which is seen in the bottom right, the nonlinearity values for most pixels are not expected to be measurable because of the small local flux. For ease of identifying other behaviors, inoperable pixels and pixels for which nonlinearities were not measured are depicted as white in this figure. There are two red rings of pixels exhibiting the constant capacitance behavior, which are centered around the bright circles seen in (d), a pedestal image of the same area, further suggesting a nearest neighbor interaction as the source of the constant capacitance behavior.

Additional instances of this behavior can be seen in other arrays, such as H2RG-20071, a 10.1 μm cutoff engineering-grade device, for which a portion of the standard deviation map is shown in Fig. 7c. The bottom right corner of this figure shows the outer edge of the vignetted illumination pattern produced by the Rochester

experimental set up. Beyond this illumination pattern, nonlinearity values are not measured for most pixels because the local light intensity is too low to produce a large enough fluence range in the sampled integration time for the nonlinearity measurement. As a result, any measured values outside of this pattern are expected to be steeper nonlinearities, which would be depicted as blue, that belong to pixels with large enough dark currents to pass the applied bias threshold in dim illumination. For ease of identifying the red and blue behaviors, inoperable pixels and pixels outside of this central illumination pattern for which the nonlinearity is not measured because of low fluence are depicted as white in this figure. Instead of exclusively measuring steep nonlinearities associated with high dark current pixels, there are two red rings of constant capacitance behavior observed beyond the illumination pattern. Comparing this map to a pedestal image of the same region (Fig. 7d), shows these bright red rings occur around two circular regions of especially bright pixels, providing further support for the constant capacitance behavior to be caused by a nearest neighbor interaction between pixels that saturate quickly and their neighbors.

In addition to the constant capacitance behavior, for which the FF curves for all pixels in this group in H2RG-18693 are shown in Fig. 8a, there are two other common deviations from the expected FF behavior, both of which occur at the high signal end. Figure 8b shows a pixel that initially follows the expected FF behavior before seeing a spontaneous increase in signal rate, matching the anomalous upturn seen in Fig. 5a. The onset signal and amplitude of the signal rate increase is repeatable between the two included trials. Similarly, Fig. 8c shows a pixel with a large initial dark current that decays to the expected behavior before saturating. While saturated, however, the pixel spontaneously begins collecting more charge and moves to a higher saturation level. The onset time and amplitude of the signal shift is repeatable between both trials despite nothing changing within the pixel of interest.

More information behind the onset of these features can be discerned by plotting the discrete time derivative of the measured signal for a pixel and its neighbors, such as is shown in Fig. 9. In this figure, a central pixel (blue) has a large initial tunneling dark current that causes it to saturate before all of its nearest neighbors (red triangles) at the first vertical dashed line. At this point, all four neighbors deviate away from the expected FF behavior they had been previously following and begin exhibiting the high signal bump. Similarly, at the moment three of the four neighbors of the central pixel saturate at the second vertical dashed line, the central saturated pixel sees an increase in signal rate as it shifts further into forward bias to a second higher saturation level. The remaining unsaturated neighbor (down-facing triangle) also sees an uncharacteristically large jump across this second vertical line.

The high signal bump can easily be explained as an increase in the local incoming signal rate, but so too can the two-level saturation feature. Pixels in these arrays saturate in forward bias and the final saturation voltage depends on the intensity of the incoming signal rate, with larger fluxes pushing the pixel further into forward bias. If an already saturated pixel encounters a large change in incoming signal rate, the established equilibrium will be disturbed and the saturation voltage will shift to establish a new equilibrium based on the new incoming rate. An example of this behavior is shown in Fig. 10 where two pixels shift between two saturation levels in response to changing incoming signal rates. In addition, the pixel in Fig. 10b moves from its initial saturated position to a higher saturation level when the incoming signal rate increases, and begins returning towards its initial saturation level when the incoming signal rate is decreased towards its initial value.

With both the high signal bump and the two level saturation feature explainable as an instantaneous increase in the incoming signal rate that has a specific, repeatable onset when a neighboring pixel begins to saturate, a nearest neighbor interaction where a saturated pixel shares signal with its neighbors is a likely culprit. This type of interaction can also explain the constant capacitance behavior observed in Fig. 7b and Fig. 8a. The pixels whose neighbors exhibit this behavior are a class of inoperable pixel with dark currents large enough to saturate on their own prior to the frames used to measure the nonlinearity of their neighbors, meaning they would be sharing signal for all frames used in the nonlinearity measurement. In order to overcome the natural nonlinearity and create a constant capacitance behavior, the amount of signal being shared would need to increase throughout the integration time. The exact nature of this new nearest neighbor interaction, including experimental proof of the mechanism of sharing, measurements of the amplitude of charge sharing, and potential correction methods, will be discussed in an upcoming paper currently in preparation.

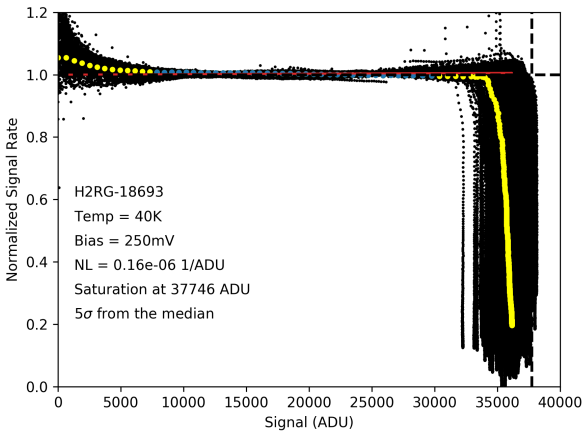

(a)

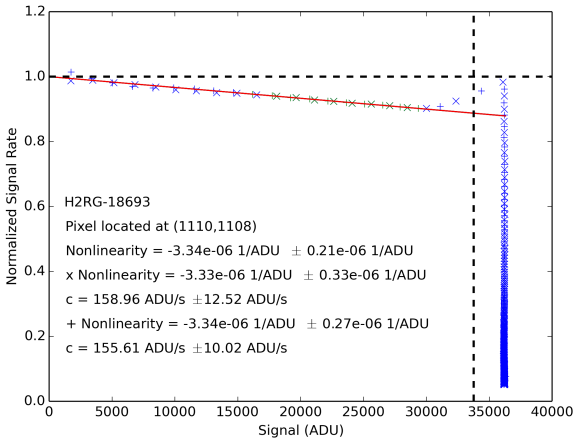

(b)

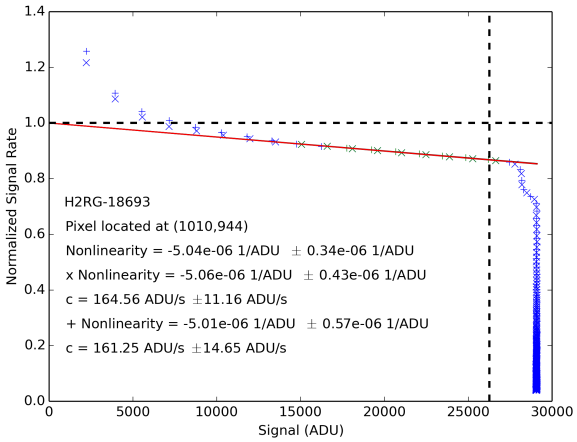

(c)

Figure 8: (a) The FF curves for all pixels in H2RG-18693 with measured nonlinearities 5 standard deviations above the median. These pixels follow the idealized constant capacitance behavior of zero nonlinearity, and occur exclusively around inoperable pixels. These pixels are represented as the bright red pixels in Fig. 7b. ((b)-(c)) Two examples of repeatable deviations from the expected linear behavior of FF curves. (b) A high signal bump where the pixel sees a spontaneous increase in signal rate that is repeatable between trials in both onset time and amplitude. (c) A two level saturation feature where the already saturated pixel shifts to a higher saturation level despite nothing appearing to change within the pixel. Both the onset time and amplitude of the shift are repeated between trials.

5. SUMMARY

Although each read of an H2RG array gives the voltage across every pixel, most end users of the devices want to know the number of charges collected during an integration time, requiring a unit conversion involving a capacitance. Unfortunately, this capacitance is not constant throughout an integration time, but increases as the depletion region width around the p-n junction decreases in response to the pixel accumulating charge. This increasing capacitance manifests as a decreasing signal rate and ignoring this nonlinear signal response can lead to significantly underestimating the total number of charges collected in an integration time.

A theoretical framework is presented to explain two methods of measuring this nonlinearity using flux vs.

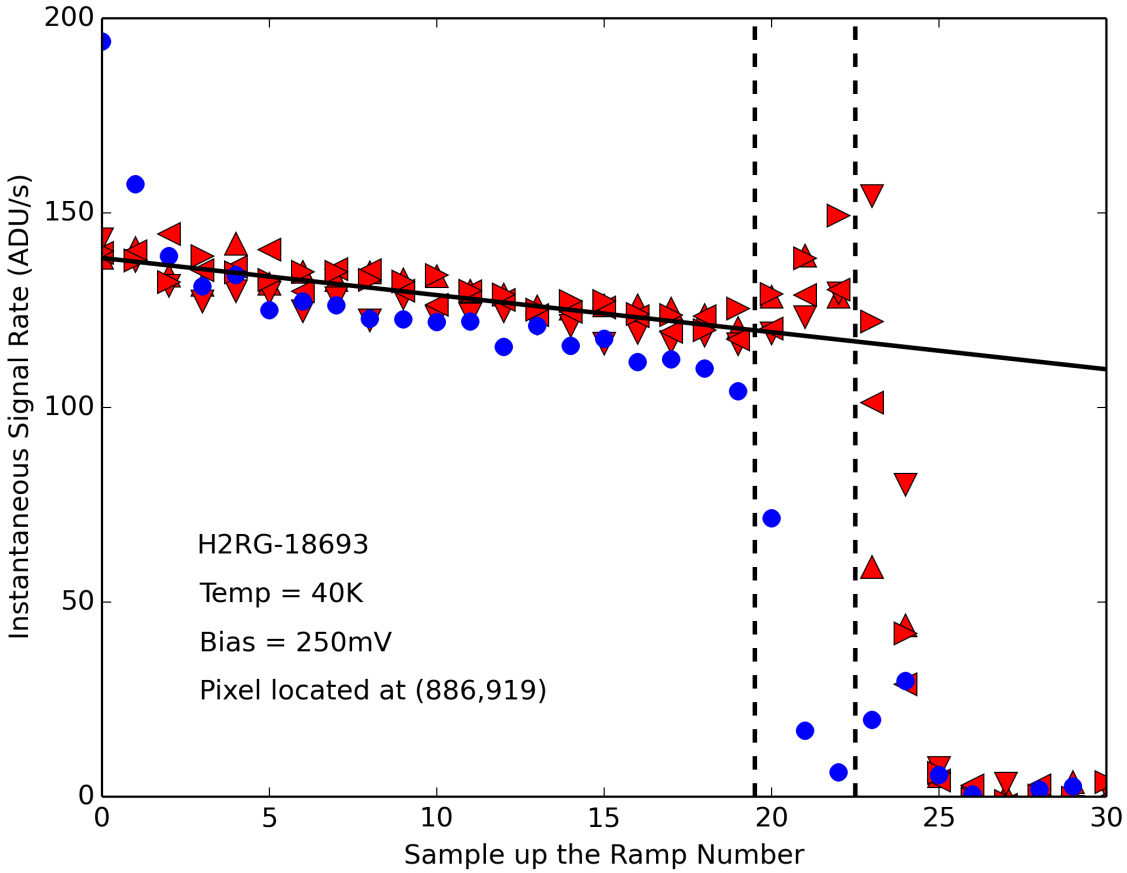

Figure 9: Discrete time derivatives of the signal for a central pixel, blue circles, and its four nearest neighbors, red triangles which point in the direction of the corresponding neighbor. The first vertical line marks when the central pixel saturates, and the second vertical line marks when the first neighbor saturates. The bold line shows the general FF trend of all neighbors to help identify when the instantaneous signal rates deviate from the expected behaviors. The instantaneous signal rates of all four neighbors begin to increase as soon as the central pixel reaches saturation. Similarly, when three of the four neighbors saturate, the central pixel, which had already saturated, exhibits a bump in signal rate as it begins to accumulate more charge moving to a second, higher saturation level. Onset of both the high signal bump and the two-level saturation feature coincide with a neighboring pixel reaching saturation.

fluence curves. Simulations show multiple curves are needed to reduce the impact of correlated Poissonian photon shot noise. Typical values of this nonlinearity are on the order of -2×10^{-6} or -3×10^{-6} 1/ADU, where 1 ADU is equal to 7.7 μV with the laboratory setup used at the University of Rochester. The fraction of charges missed by using a constant capacitance can be calculated with $f = -NM$, where N is the measured nonlinearity and M is the measured signal value. With typical (uncorrected) well depths on the order of 35,000 ADU for 250 mV of applied bias, this fraction is about 10% near the well depth. Missing 10% of the total number of detected photons would exceed the photometric calibration requirements for NEO Surveyor, making signal nonlinearity measurements a crucial portion of detector calibration and characterization. Two nonlinearity correction methods are also detailed here, one method which works for correcting CDS images and one method that works for missions where only the slopes of signal vs. time data are downlinked.

Additionally, early evidence is presented for the existence of a new nearest neighbor interaction characterized

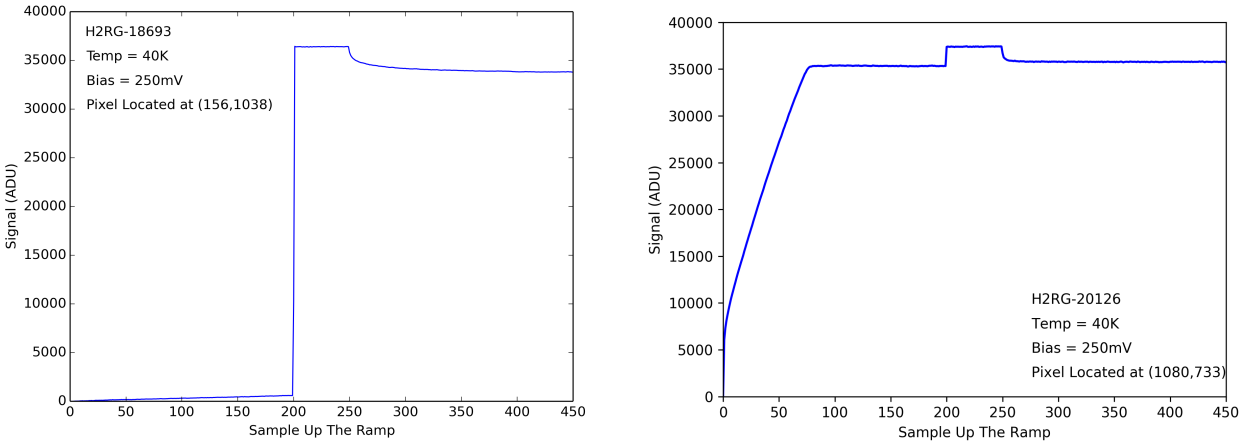

(a) (b)

Figure 10: Signal vs. frame number for (a) a pixel in H2RG-18693 with a low dark current and (b) a pixel in H2RG-20126 with a large dark current. In both cases, the pixels are initially in the dark for the first 200 frames before being placed in the light at frame 200 to saturate the pixel in forward bias and then placed back in the dark at frame 250 to allow the voltage across the pixel to decay towards the zero bias level. This data set is used to measure the dark current and well depth for each pixel, the results of which are shown in Fig. 1, where the dark current is the initial slope of the signal vs. time data and the well depth is the final saturation voltage after being placed back in the dark. The pixel in (b) has a dark current large enough to saturate from dark current alone. At frame 200, the already saturated pixel shifts to a higher saturation level in response to the changing incoming signal rate when placed in the light. When placed placed back in the dark at frame 250, the voltage across the pixel begins to decay towards the initial saturation level.

by a saturated pixel sharing signal with its neighbors. A full investigation of this effect will be described in an upcoming paper currently in preparation.

ACKNOWLEDGMENTS

The authors would like to thank Donald Lee of Teledyne Imaging Sensors and Peter Eisenhardt of the Jet Propulsion Laboratory for their contribution to this work. Additionally, the authors would like to acknowledge financial support from Cornell University through New York Space Grant 80NSSC20M0096, the Jet Propulsion Laboratory through the Near Earth Object Camera (NEOCam) Extended Phase A Subcontract 1573311, and the University of Arizona through the Near Earth Object Surveillance Mission (NEOSM) Extended Phase A grant 80MSFC20C0045.

REFERENCES

[1] Mainzer, A. K., "NEOCam: The Near-Earth Object Camera," in [*AAS/Division for Planetary Sciences Meeting Abstracts #38*], *AAS/Division for Planetary Sciences Meeting Abstracts* **38**, 45.09 (Sept. 2006).

[2] Brown, P. G., Assink, J. D., Astiz, L., Blaauw, R., Boslough, M. B., Borovička, J., Brachet, N., Brown, D., Campbell-Brown, M., Ceranna, L., Cooke, W., de Groot-Hedlin, C., Drob, D. P., Edwards, W., Evers, L. G., Garces, M., Gill, J., Hedlin, M., Kingery, A., Laske, G., Le Pichon, A., Mialle, P., Moser, D. E., Saffer, A., Silber, E., Smets, P., Spalding, R. E., Spurný, P., Tagliaferri, E., Uren, D., Weryk, R. J., Whitaker, R., and Krzeminski, Z., "A 500-kiloton airburst over Chelyabinsk and an enhanced hazard from small impactors," *Nature* **503**, 238–241 (Nov. 2013). [doi:10.1038/nature12741].

[3] United States Congress, "George E. Brown, Jr. Near-Earth Object Survey Act, Public Law 109-155 Sec. 321 42 ." U.S.C. 16691, December 30 2005 https://www.congress.gov/109/plaws/publ155/PLAW-109publ155.pdf (2005). (Accessed: 30 November 2020).

[4] Stokes, G. H., Barbee, B. W., William F. Bottke, J., Buie, M. W., Chesley, S. R., Chodas, P. W., Evans, J. B., Gold, R. E., Grav, T., Harris, A. W., Jedicke, R., Mainzer, A. K., Mathias, D. L., Spahr, T. B., and Yeomans, D. K., "Update to Determine the Feasibility of Enhancing the Search and Characterization of NEOs." Report of the Near-Earth Object Science Definition, September 2017 https://cneos.jpl.nasa.gov/doc/2017_neo_sdt_final_e-version.pdf (2017). (Accessed: 30 November 2020).

[5] Mainzer, A., Grav, T., Bauer, J., Conrow, T., Cutri, R. M., Dailey, J., Fowler, J., Giorgini, J., Jarrett, T., Masiero, J., Spahr, T., Statler, T., and Wright, E. L., "SURVEY SIMULATIONS OF a NEW NEAR-EARTH ASTEROID DETECTION SYSTEM," *The Astronomical Journal* **149**, 172 (apr 2015). [doi:10.1088/0004-6256/149/5/172].

[6] Minor Planet Center, "MPEC 2019-O56: 2019 OK." Minor Planet Electronic Circular, 24 July 2019 https://minorplanetcenter.net/mpec/K19/K19O56.html (2019). (Accessed: 30 November 2020).

[7] Jet Propulsion Laboratory, "2019 OK." JPL Small-Body Database Browser, 31 May 2020 https://ssd.jpl.nasa.gov/sbdb.cgi?sstr=2019%20OK;old=0;orb=0;cov=0;log=0;cad=1#cad (2019). (Accessed: 30 November 2020).

[8] Shoemaker, E. M., "Asteroid and comet bombardment of the earth," *Annual Review of Earth and Planetary Sciences* **11**(1), 461–494 (1983). [doi:10.1146/annurev.ea.11.050183.002333].

[9] Mainzer, A., Bauer, J., Grav, T., Masiero, J., Cutri, R. M., Dailey, J., Eisenhardt, P., McMillan, R. S., Wright, E., Walker, R., Jedicke, R., Spahr, T., Tholen, D., Alles, R., Beck, R., Brand enburg, H., Conrow, T., Evans, T., Fowler, J., Jarrett, T., Marsh, K., Masci, F., McCallon, H., Wheelock, S., Wittman, M., Wyatt, P., DeBaun, E., Elliott, G., Elsbury, D., Gautier, T., I., Gomillion, S., Leisawitz, D., Maleszewski, C., Micheli, M., and Wilkins, A., "Preliminary Results from NEOWISE: An Enhancement to the Wide-field Infrared Survey Explorer for Solar System Science," **731**, 53 (Apr. 2011). [doi:10.1088/0004-637X/731/1/53].

[10] Wright, E. L., Eisenhardt, P. R. M., Mainzer, A. K., Ressler, M. E., Cutri, R. M., Jarrett, T., Kirkpatrick, J. D., Padgett, D., McMillan, R. S., Skrutskie, M., Stanford, S. A., Cohen, M., Walker, R. G., Mather, J. C., Leisawitz, D., Gautier, T. N., McLean, I., Benford, D., Lonsdale, C. J., Blain, A., Mendez, B., Irace, W. R., Duval, V., Liu, F., Royer, D., Heinrichsen, I., Howard, J., Shannon, M., Kendall, M., Walsh, A. L., Larsen, M., Cardon, J. G., Schick, S., Schwalm, M., Abid, M., Fabinsky, B., Naes, L., and Tsai, C.-W., "THE WIDE-FIELD INFRARED SURVEY EXPLORER (WISE): MISSION DESCRIPTION AND INITIAL ON-ORBIT PERFORMANCE," *The Astronomical Journal* **140**, 1868–1881 (nov 2010). [doi:10.1088/0004-6256/140/6/1868].

[11] Loose, M., Farris, M. C., Garnett, J. D., Hall, D. N. B., and Kozlowski, L. J., "HAWAII-2RG: a 2kx2k CMOS multiplexer for low- and high-background astronomy applications," in [*IR Space Telescopes and Instruments*], Mather, J. C., ed., **4850**, 867 – 879, International Society for Optics and Photonics, SPIE (2003). [doi:10.1117/12.461796].

[12] McMurty, C., Lee, D. L., Beletic, J., Chen, C.-Y. A., Demers, R. T., Dorn, M., Edwall, D. D., Fazar, C. M., Forrest, W. J., Liu, F., Mainzer, A. K., Pipher, J. L., and Yulius, A., "Development of sensitive long-wave infrared detector arrays for passively cooled space missions," *Optical Engineering* **52**(9), 1 – 10 (2013). [doi:10.1117/1.OE.52.9.091804].

[13] Ressler, M. E., Cho, H., Lee, R. A. M., Sukhatme, K. G., Drab, J. J., Domingo, G., McKelvey, M. E., Jr., R. E. M., and Dotson, J. L., "Performance of the JWST/MIRI Si:As detectors," in [*High Energy, Optical, and Infrared Detectors for Astronomy III*], Dorn, D. A. and Holland, A. D., eds., **7021**, 224 – 235, International Society for Optics and Photonics, SPIE (2008). [doi:10.1117/12.789606].

[14] Martinka, M., Almeida, L. A., Benson, J. D., and Dinan, J. H., "Characterization of cross-hatch morphology of MBE (211) HgCdTe," *Journal of Electronic Materials* **30**(6), 632–636 (2001). [doi:10.1007/BF02665847].

[15] Carmody, M., Pasko, J. G., Edwall, D., Bailey, R., Arias, J., Cabelli, S., Bajaj, J., Almeida, L. A., Dinan, J. H., Groenert, M., Stoltz, A. J., Chen, Y., Brill, G., and Dhar, N. K., "Molecular beam epitaxy grown long wavelength infrared HgCdTe on Si detector performance," *Journal of Electronic Materials* **34**(6), 832–838 (2005). [doi:10.1007/s11664-005-0028-2].

[16] Chang, Y., Becker, C. R., Grein, C. H., Zhao, J., Fulk, C., Casselman, T., Kiran, R., Wang, X. J., Robinson, E., An, S. Y., Mallick, S., Sivananthan, S., Aoki, T., Wang, C. Z., Smith, D. J., Velicu, S., Zhao, J., Crocco, J., Chen, Y., Brill, G., Wijewarnasuriya, P. S., Dhar, N., Sporken, R., and Nathan,

V., "Surface morphology and defect formation mechanisms for HgCdTe (211)B grown by molecular beam epitaxy," *Journal of Electronic Materials* **37**(9), 1171–1183 (2008). [doi:10.1007/s11664-008-0477-5].

[17] Cabrera, M. S., McMurtry, C. W., Dorn, M. L., Forrest, W. J., Pipher, J. L., and Lee, D. L., "Development of 13-μm cutoff HgCdTe detector arrays for astronomy," *Journal of Astronomical Telescopes, Instruments, and Systems* **5**(3), 1 – 18 (2019). [doi:10.1117/1.JATIS.5.3.036005].

[18] Cabrera, M. S., McMurtry, C. W., Forrest, W. J., Pipher, J. L., Dorn, M. L., and Lee, D. L., "Characterization of a 15- μm cutoff HgCdTe detector array for astronomy," *Journal of Astronomical Telescopes, Instruments, and Systems* **6**(1), 1 – 9 (2019). [doi:10.1117/1.JATIS.6.1.011004].

[19] Fowler, A. M. and Gatley, I., "Demonstration of an Algorithm for Read-Noise Reduction in Infrared Arrays," **353**, L33 (Apr. 1990). [doi:10.1086/185701].

[20] Garnett, J. D. and Forrest, W. J., "Multiply sampled read-limited and background-limited noise performance," in [*Infrared Detectors and Instrumentation*], Fowler, A. M., ed., **1946**, 395 – 404, International Society for Optics and Photonics, SPIE (1993). [doi:10.1117/12.158692].

[21] Mortara, L. and Fowler, A., "Evaluations Of Charge-Coupled Device (CCD) Performance For Astronomical Use," in [*Solid-State Imagers for Astronomy*], Geary, J. C. and Latham, D. W., eds., **0290**, 28 – 33, International Society for Optics and Photonics, SPIE (1981). [doi:10.1117/12.965833].

[22] Moore, A. C., Ninkov, Z., and Forrest, W. J., "Interpixel capacitance in nondestructive focal plane arrays," in [*Focal Plane Arrays for Space Telescopes*], Grycewicz, T. J. and McCreight, C. R., eds., **5167**, 204 – 215, International Society for Optics and Photonics, SPIE (2004). [doi:10.1117/12.507330].

[23] Donlon, K., Ninkov, Z., and Baum, S., "Signal dependence of inter-pixel capacitance in hybridized HgCdTe H2RG arrays for use in James Webb space telescope's NIRcam," in [*High Energy, Optical, and Infrared Detectors for Astronomy VII*], Holland, A. D. and Beletic, J., eds., **9915**, 807 – 814, International Society for Optics and Photonics, SPIE (2016). [doi:10.1117/12.2233200].